The Astrophysical Journal, 768:47 (8pp), 2013 May 1 doi:10.1088/0004-637X/768/1/47

SN 2009ip: CONSTRAINTS ON THE PROGENITOR MASS-LOSS RATE

E. O. Ofek[1], L. Lin[2], C. Kouveliotou[3], G. Younes[4], E. Göğüş[2], M. M. Kasliwal[5], and Y. Cao[6]
[1] Benoziyo Center for Astrophysics and the Helen Kimmel Center for Planetary Science, Weizmann Institute of Science, 76100 Rehovot, Israel
[2] Faculty of Engineering and Natural Sciences, Sabancı University, Orhanlı-Tuzla, İstanbul 34956, Turkey
[3] Space Science Office, ZP-12, NASA/Marshall Space Flight Center, Huntsville, AL 35812, USA
[4] Universities Space Research Association, 6767 Old Madison Pike NW, Suite 450, Huntsville, AL 35806, USA
[5] Observatories of the Carnegie Institution for Science, 813 Santa Barbara St, Pasadena, CA 91101, USA
[6] Division of Physics, Mathematics and Astronomy, California Institute of Technology, Pasadena, CA 91125, USA
Received 2013 January 14; accepted 2013 March 14; published 2013 April 12

ABSTRACT

Some supernovae (SNe) show evidence for mass-loss events taking place prior to their explosions. Measuring their pre-outburst mass-loss rates provides essential information regarding the mechanisms that are responsible for these events. Here we present *XMM-Newton* and *Swift* X-ray observations taken after the latest, and presumably the final, outburst of SN 2009ip. We use these observations as well as new near-infrared and visible-light spectra and published radio and visible-light observations to put six independent order-of-magnitude constraints on the mass-loss rate of the SN progenitor prior to the explosion. Our methods utilize the X-ray luminosity, the bound–free absorption, the Hα luminosity, the SN rise time, free–free absorption, and the bolometric luminosity of the outburst detected prior to the explosion. Assuming spherical mass loss with a wind-density profile, we estimate that the effective mass-loss rate from the progenitor was between 10^{-3} and 10^{-2} $M_{\odot}$ yr^{-1}, over a few years prior to the explosion, with a velocity of $\sim 10^{3}$ km s^{-1}. This mass-loss rate corresponds to a total circumstellar matter (CSM) mass of $\sim$0.04 $M_{\odot}$, within 6×10^{15} cm of the SN. We note that the mass-loss rate estimate based on the Hα luminosity is higher by an order of magnitude. This can be explained if the narrow-line Hα component is generated at radii larger than the shock radius, or if the CSM has an aspherical geometry. We discuss simple geometries which are consistent with our results.

Key words: stars: mass-loss – supernovae: general – supernovae: individual (SN 2009ip)

Online-only material: machine-readable table

1. INTRODUCTION

Supernova (SN) observations, especially of Type IIn (e.g., Filippenko 1997), indicate that some massive stars lose considerable amounts of mass ($\gtrsim 10^{-4}$ $M_{\odot}$) within a few months to years prior to their explosions (e.g., Dopita et al. 1984; Chugai & Danziger 1994; Chugai et al. 2004; Ofek et al. 2007, 2010, 2013b; Smith et al. 2007, 2008, 2009; Kiewe et al. 2012). Several theoretical mechanisms to eject large amounts of mass with super-Eddington luminosities have been suggested. Quataert & Shiode (2012) suggest that in some massive stars the super-Eddington fusion luminosities, shortly prior to core collapse, can drive convective motions, which in turn excite gravity waves that propagate toward the stellar surface. The dissipation of these waves can unbind up to several solar masses of the stellar envelope. In Ofek et al. (2013b), we argued that this mechanism can unbind a lower amount of mass ($\sim 10^{-2}$ $M_{\odot}$). Arnett & Meakin (2011) suggested that shell oxygen burning in massive stars produces large fluctuations in the turbulent kinetic energy, which in turn may produce bursts. Chevalier (2012) suggested that the mass loss is driven by a common-envelope phase due to the inspiral of a neutron star into a giant companion core, unbinding the companion envelope and setting up accretion onto the neutron star, which in turn collapses into a black hole and triggers an SN explosion. Soker & Kashi (2013) suggested that the SN 2009ip explosion was due to the merger of two stars, while some of the pre-explosion outbursts occurred near periastron passages of the binary system. Another possible mechanism is the pulsational pair instability which in very massive stars can generate several explosions, expelling $\gtrsim 1$ $M_{\odot}$ each, followed by the collapse of the stellar core (Rakavy et al. 1967; Woosley et al. 2007; Waldman 2008).

Measuring the mass-loss rates from massive stars prior to their explosion can be used as a tool to study the latest stages of stellar evolution, and to discriminate between the different models suggested to generate large mass-loss events. Objects in which super-Eddington outbursts were directly observed prior to the SN explosion provide a way to constrain the time at which mass loss was taking place, and relate the optical luminosities with mass-loss rates and kinetic energy estimates. To date there are only three SNe in which precursor outbursts were seen prior to the SN explosion. These are the Type Ibn SN 2006jc (e.g., Foley et al. 2007; Pastorello et al. 2008), the Type IIn SN 2009ip (e.g., Mauerhan et al. 2013; Pastorello et al. 2013; Prieto et al. 2013), and the Type IIn SN 2010mc/PTF 10tel (Ofek et al. 2013b).

Here we present *XMM-Newton* and *Swift* X-ray observations of SN 2009ip. We use these observations as well as published and new visible-light and radio observations to set an order-of-magnitude estimate on the mass loss prior to the SN explosion.

SN 2009ip was a luminous blue variable (LBV) originally detected in the outburst on 2009 August 26.11 by the CHASE survey at a projected distance of 4.3 kpc from NGC 7259 (Maza et al. 2009). Three additional outbursts were subsequently discovered with the Catalina Real-Time Transient Survey on 2010 July 15, on 2010 September 29 (Drake et al. 2010), and then again on 2012 July 24 (Drake et al. 2012). Based on its multiple outbursts, Smith et al. (2010) and Foley et al. (2011) argued that it is an SN impostor (see recent reviews in Kochanek et al. 2012; Smith et al. 2011; van Dyk & Matheson 2012). On 2012 September, Smith & Mauerhan (2012), and later Mauerhan et al. (2013), reported the detection of broad P Cygni lines with velocities of up to 13,000 km s^{-1}, suggesting that the star had finally exploded as a Type IIn SN. Previous cases in which a

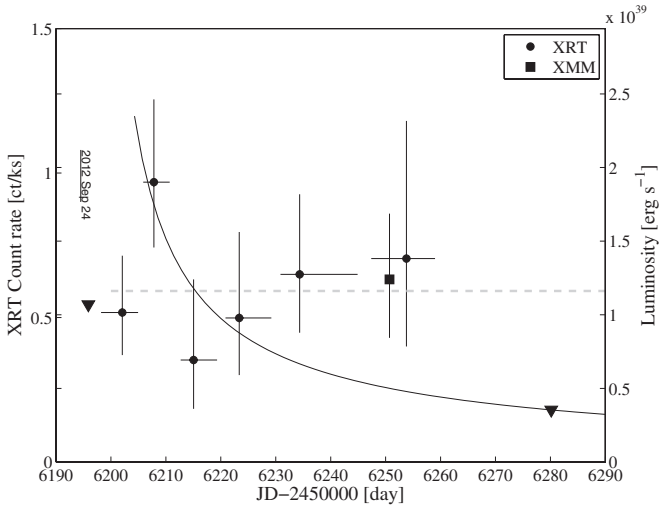

Figure 1. X-ray light curve of SN 2009ip based on *Swift*-XRT (circles) and *XMM-Newton* (square) observations. The triangles mark XRT 2σ upper limit. The horizontal error bars represent the range of observations in each bin. The gray dashed line indicates the mean XRT count rate level of the observations taken between 2012 September 29 and 2012 November 28. It corresponds to a luminosity of $\approx 1.1 \times 10^{39}$ erg s^{-1}. We note that the left-hand axis count rate corresponds only to the *Swift*-XRT observations. The right-hand axis shows the unabsorbed luminosity assuming a Galactic hydrogen column density of $N_{\rm H} = 1.2 \times 10^{20}$ cm^{-2} and an X-ray spectrum of the form $n(E) \propto E^{-1.8}$, where $n(E)$ is the photon numbers per unit energy. The black solid line shows the expected, order of magnitude, evolution of the X-ray luminosity assuming optically thin wind-profile CSM with mass-loss rate of $7 \times 10^{-4}\ M_{\odot}$ yr^{-1} and $v_w = 500$ km s^{-1} (based on Equations (8) and (12)).

likely LBV progenitor has exploded as an SN include SN 2005gl (Gal-Yam et al. 2007; Gal-Yam & Leonard 2009) and SN 1961V (Kochanek et al. 2011; Smith et al. 2011). Prieto et al. (2013) reported that around 2012 September 24 the object's I-band light curve started to rise rapidly at a rate of 2.3 mag day^{-1}. Shortly afterward, on early October, X-ray emission was detected from SN 2009ip with the *Swift*/X-Ray Telescope (XRT; Margutti & Soderberg 2012b).

Throughout the paper we assume that the source is located at a distance of 20.4 Mpc. In Section 2 we present our observations of SN 2009ip, while in Section 3 we review various methods for estimating the mass content of the SN circumstellar matter (CSM). Finally, in Section 4 we apply these methods to SN 2009ip and discuss our findings.

2. OBSERVATIONS

We observed SN 2009ip with *XMM-Newton* on 2012 November 1 in prime full-window imaging mode for an effective exposure time of 8 ks. Using data collected with the EPIC-pn detector, we accumulated the source spectrum from a circular region of 30″ centered on the optical position of SN 2009ip. We selected a circular background region from a source-free area on the same chip (i.e., CCD 7) with the same aperture size. The source is detected at a significance of about 3σ with a background-subtracted count rate of $(4.6 \pm 1.5) \times 10^{-3}$ counts s^{-1}, yielding a total of 37 net source counts in the 0.5–10 keV. We generated the detector and ancillary response files using the latest calibration data.

The *Swift*-XRT (Gehrels et al. 2004) observed SN 2009ip on an almost daily basis since 2012 September 4 (triggered by Roming/Maragutti). Some of these X-ray observations have been already reported in, e.g., Margutti et al. (2012) and Campana (2012). For each *Swift*-XRT image of the SN, we extracted the number of X-ray counts in the 0.2–10 keV band within an aperture of 9″ radius centered on the SN position. We note that this aperture contains ≈50% of the source flux (Moretti et al. 2004). The background count rates were estimated in annuls around the SN location, with an inner (outer) radius of 50″ (100″). The log of *Swift*-XRT observations, along with the source and background X-ray counts in the individual observations, is listed in Table 1. SN 2009ip is only marginally detected in individual images, but it is clearly visible in the co-added data. Figure 1 shows a binned light curve based on the *Swift*-XRT observations. The binned measurements are listed in Table 2.

For our XRT spectral analysis we selected all the XRT observations between MJD 56174 and 56228, taken in photon-counting mode and with an integration longer than 500 s. This resulted in a total effective exposure time of 149 ks. We extracted a stacked source spectrum from a circular region centered at the SN location with a radius of 20″. The stacked background spectrum was accumulated from a 20″ circular source-free region for all observations. We grouped the source spectrum with a minimum of 10 counts in each energy bin.

Table 1
Swift-XRT Observations

MJD (days)	Exposure Time (ks)	Source (counts)	Background (counts)
55084.44	9.86	0	19
56174.86	1.96	0	4
56176.60	1.78	0	4
56183.40	1.65	0	4
56190.75	0.39	0	0

Notes. MJD is the modified Julian day. Source is the number of counts in a 9″ radius aperture of the source position and in the 0.2–10 keV band. Background is the number of counts in the 0.2–10 keV band, in an annuls of inner (outer) radius of 50″ (100″) around the source. The ratio between the background annulus area and the aperture area is 92.59.

(This table is available in its entirety in a machine-readable form in the online journal. A portion is shown here for guidance regarding its form and content.)

Table 2
Swift-XRT Binned Data

⟨MJD⟩	Range		CR	$UL_{2\sigma}$	Exp.
(days)	(days)	(days)	(counts ks^{-1})	(counts ks^{-1})	(ks)
55084.4	−0.0	0.0	...	0.61	9.86
56178.0	−3.2	12.7	...	1.03	5.79
56195.4	−2.7	2.0	...	0.55	17.40
56201.6	−3.9	2.9	$0.52^{+0.20}_{-0.15}$	...	46.38
56207.3	−1.9	2.9	$0.97^{+0.29}_{-0.23}$	...	37.17
56214.5	−2.3	4.3	$0.35^{+0.28}_{-0.17}$	...	22.66
56222.8	−2.5	5.9	$0.50^{+0.30}_{-0.20}$	...	24.08
56233.9	−3.5	10.5	$0.65^{+0.28}_{-0.20}$	...	30.80
56253.3	−6.4	5.2	$0.70^{+0.48}_{-0.30}$	...	14.20
56279.7	−19.4	14.7	...	0.18	52.57

Notes. Binned *Swift*-XRT light curve of SN 2009ip. ⟨MJD⟩ is the weighted mean modified Julian day of all the observations in a given bin, where the observations are weighted by their exposure times. Range is the time range around ⟨MJD⟩ in which the light curve (Table 1) was binned. CR is the count rate along with the lower and upper 1σ errors. We note that the source count rates are corrected for extraction aperture losses. $UL_{2\sigma}$ is the 2σ upper limit on the source count rate, which is given if the total source count within the binned exposure is $\leqslant 1$. Exp. is the exposure time.

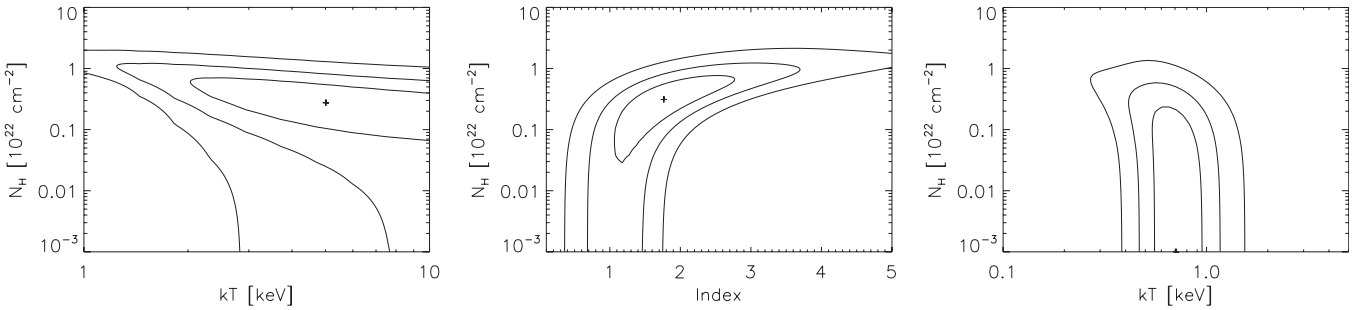

Figure 2. Left: $\Delta\chi^2$ contours for fitting the *XMM* and *Swift*-XRT spectra with a Mekal model in the column density vs. temperature (kT) space (see the text for details). The contours represent the 1σ, 2σ, and 3σ errors, while the plus sign represents the best-fit model. Middle: same as the left panel, but for a power-law model. The *X*-axis represents the power-law index, Γ. Right: same as the left panel, but for a blackbody model. The *X*-axis represents the blackbody temperature in keV.

Table 3
X-Ray Spectral Parameters

Model	Parameter	$N_{\rm H}$ (cm^{-2})	χ^2/dof
Mekal	$kT = 4.74^{+18}_{-2.3}$ keV	$(2.8^{+2.4}_{-1.6}) \times 10^{21}$	14.66/13
Power law	$\Gamma = 1.79^{+0.60}_{-0.50}$	$(3.2^{+2.7}_{-2.0}) \times 10^{21}$	14.98/13
Blackbody	$kT = 0.72 \pm 0.10$ keV	...	18.19/13

Notes. Γ is defined as the power-law index in a spectrum of the form $n(E) \propto E^{-\Gamma}$, where $n(E)$ is the number of photons per unit energy. dof is the number of degrees of freedom.

The background-subtracted count rate of the source is $(4.1 \pm 0.7) \times 10^{-4}$ counts s^{-1}, corresponding to 61 net source counts.

We used XSPEC[7] V12.7.1 (Schafer 1991) to simultaneously fit the *XMM* and *Swift*-XRT spectra. In all cases we set the Galactic extinction to $N_{\rm H} = 1.2 \times 10^{20}$ cm^{-2} (Dickey & Lockman 1990), and we fitted four parameters: normalization of the *XMM* spectrum, normalization of the *Swift*-XRT spectrum, a parameter describing the spectrum (i.e., temperature or power-law index), and the hydrogen column density at the redshift of the SN ($z = 0.00594$) assuming solar metallicity. The best-fit parameters are listed in Table 3.

Figure 2 shows the $\Delta\chi^2$ contours of these fits in the $N_{\rm H}$ versus temperature (kT) or power-law index space. From these fits we can set a 3σ upper limit on $N_{\rm H}$ in the SN CSM of 2×10^{22} cm^{-2}.

On 2012 September 22, two days before the fast rise in the light curve, we obtained a near-infrared (NIR) spectrum of SN 2009ip with the Folded-port InfraRed Echellette spectrograph (FIRE; Simcoe et al. 2008, 2010) on the 6.5 m Magellan Baade Telescope. We used the low-dispersion, high-throughput prism mode and completed an ABBA dither sequence. The data span 0.8–2.5 μm at a resolution ranging from 300 to 500. Immediately afterward, we obtained a spectrum of an A0V standard star for the purposes of flux calibration and removal of telluric absorption features, as described in Vacca et al. (2003). Data were reduced using the FIREHOSE pipeline developed by R. Simcoe, J. Bochanski, and M. Matejek. Smith et al. (2013) present a detailed analysis of the NIR spectrum.

On 2012 December 4, we obtained a visible-light spectrum of SN 2009ip using the Dual Imaging Spectrograph (DIS) mounted on the ARC 3.5 m telescope at Apache Point Observatory to obtain a spectrum, with 600 s integration, of SN 2009ip in the wavelength range from 3500 Å to 9000 Å and resolution of about 400. The visible-light spectrum was flux-calibrated using the standard star BD+28°4211. Parts of the IR and visible-light spectra, centered on the Paschen α and Hα lines, respectively, are shown in Figure 3. The full spectra are available from the WISeREP archive (Yaron & Gal-Yam 2012). We fitted a two-Gaussian model to the Paschen α and Hα lines. We find that in the Paschen α line the narrow (wide) component width corresponds to a velocity of ≈200 (≈2100) km s^{-1}. In the Hα line, the narrow-line component width corresponds to a velocity of ≈300 km s^{-1}, while the difference between the emission line center and the bottom of the P Cygni absorption feature is about 8000 km s^{-1}. The flux of the Hα narrow component is about 3×10^{-14} erg cm^{-2} s^{-1}. Since we do not have access to photometric measurements of the SN obtained around the same time in which we got the visible-light spectrum, we estimate that the line flux measurement is good to about 30%. For future calibration, we note that, based on the current calibration, the Sloan Digital Sky Survey AB synthetic magnitudes of the visible-light spectrum are 17.17, 16.31, and 16.11 in the g, r, and i bands, respectively.

3. MASS-LOSS ESTIMATORS

Here we review several methods that we use to constrain the mass-loss rate from SN progenitors. In Section 4, we implement these methods for the case of SN 2009ip.

We use several observables, including the bound–free absorption limit derived from the X-ray spectrum, the X-ray luminosity, upper limit on the diffusion timescale as derived from the SN rise time, the Hα luminosity, the non-detection in radio bands, and the bolometric luminosity of the precursor observed prior to the SN explosion.

Our model assumes that the interaction of the SN blast wave with the CSM produces X-ray and radio emission at the radius of the shock. The visible-light photons may be produced below, or at, the shock radius. The Hα emission can be emitted either at the shock region, if it is due to collisional processes, or above the shock radius if it originates from optically thin CSM ionized by the SN radiation field. All the photon diffusion and attenuation are taking place above the shock.

Throughout the paper we assume that the CSM around the progenitor has a spherical wind-density profile of the form $\rho = Kr^{-2}$, where r is the distance from the progenitor, $K \equiv \dot{M}/(4\pi v_{\rm w})$ is the mass-loading parameter, $\dot{M}$ is the mass-loss rate, and $v_{\rm w}$ is the wind/outburst velocity. Given the outbursts observed in SN 2009ip prior to its final explosion, it is likely that the CSM was not ejected as a continuous wind with a uniform velocity. However, the mass-loss rate estimators we use below are not very sensitive to this assumption. The reason for this is that, for a reasonable density distribution, the emission, or attenuation, is calculated by integrals which are dominated

[7] http://heasarc.gsfc.nasa.gov/xanadu/xspec/

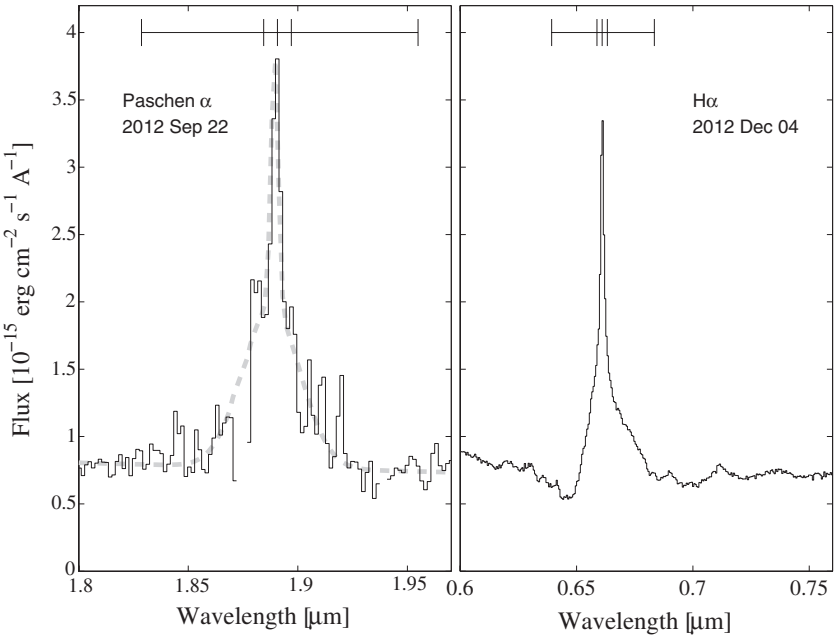

Figure 3. Left: near-IR spectrum of SN 2009ip. The *X*-axis is the wavelength at the observer's frame. The spectrum is centered on the Paschen α line. The vertical lines on the scale correspond (from left to right) to velocities of -10^4, -10^3, 0, 10^3, and 10^4 km s^{-1} relative to the line center. The dashed gray line shows the best-fit two-Gaussian model (we note that the Gaussians were convolved with the approximate instrumental broadening). The gaps in the plot are due to the removal of bad/noisy pixels. Right: same as the left spectrum, but for the visible-light Hα line.

by the value at the shock radius. Here, the only exception is the mass-loss estimator based on the Hα line luminosity (see Section 3.2). Therefore, we argue that the use of the continuous wind-density profile provides an order-of-magnitude estimate for the mass-loss rate. In the following sections, we discuss our specific mass-loss rate estimators and their caveats.

3.1. Bound–Free Absorption

The particle density profile, in a continuous wind, is given by (e.g., Chevalier 1982)

$$n \approx \frac{1}{\langle \mu_{\rm p} \rangle} \frac{\dot{M}}{4\pi m_{\rm p} v_{\rm w} r^2} \cong 6 \times 10^8 \frac{1}{\langle \mu_{\rm p} \rangle} \dot{M}_{0.01} v_{\rm w,500}^{-1} r_{15}^{-2}\ {\rm cm}^{-3}, \quad (1)$$

where $\dot{M}_{0.01}$ is the mass-loss rate in units of $10^{-2}\ M_\odot\ {\rm yr}^{-1}$, $v_{\rm w,500}$ is the wind/outburst speed in units of 500 km s^{-1}, r_{15} is the radius in units of 10^{15} cm, $m_{\rm p}$ is the proton mass, and $\langle \mu_{\rm p} \rangle$ is the mean number of nucleons per particle (mean molecular weight). For our order-of-magnitude calculation, we adopt $\langle \mu_{\rm p} \rangle = 0.6$. In a wind profile, the column density between radius r and infinity is

$$N = \int_r^\infty n dr \approx 1 \times 10^{24} \dot{M}_{0.01} v_{\rm w,500}^{-1} r_{15}^{-1}\ {\rm cm}^{-2}. \quad (2)$$

Assuming that the gas in the pre-shocked wind is neutral and has solar abundance, the bound–free optical depth in the 0.03–10 keV region is roughly given by (e.g., Behar et al. 2011)[8]

$$\tau_{\rm bf} = N\sigma(E) \approx 60 \dot{M}_{0.01} v_{\rm w,500}^{-1} r_{15}^{-1} E_1^{-2.5}, \quad (3)$$

where $\sigma(E)$ is the bound–free cross section as a function of energy E and E_1 is the energy in keV. This approximation is valid when the material is neutral. However, since above $\sim$0.5 keV metals with a high ionization potential dominate the absorption, this formula is still valid, to an order of magnitude, above 0.5 keV when some of the inner electrons of the metals are bound (i.e., even if all the hydrogen is ionized). Chevalier & Irwin (2012) estimated that the metals will be completely ionized only above shock velocities of about 10^4 km s^{-1}.

3.2. Hα Luminosity

Assuming that the SN radiation field can ionize all the hydrogen in the CSM, the mass of the hydrogen generating the Hα line is

$$M_{\rm H} \approx \frac{m_{\rm p} L_{\rm H\alpha}}{h \nu_{\rm H} \alpha_{\rm H}^{\rm eff} n_{\rm e}}. \quad (4)$$

Here, h is the Planck constant, $L_{\rm H\alpha}$ is the Balmer Hα line luminosity, $\nu_{\rm H}$ is the line frequency (4.57×10^{14} Hz for Hα), and $\alpha_{\rm H}^{\rm eff}$ is the case-B effective recombination coefficient at 10,000 K ($\approx 8.7 \times 10^{-14}$ cm^3 s^{-1} for Hα; Osterbrock & Ferland 2006). An important caveat is that this estimate assumes that the line is generated by recombination. Any Hα radiation generated in the shocked region due to collisional processes is not included here. In order to avoid this problem we take as the line luminosity only the luminosity of the narrow line component, which we assume is due to wind above the shock region. In a wind profile, the integrated mass from radius r to r_1 is

$$M = \int_r^{r_1} 4\pi r^2 K r^{-2} dr = 4\pi K (r_1 - r) \sim 4\pi K \beta r \cong 0.006 \beta \dot{M}_{0.01} v_{\rm w,500}^{-1} r_{15}\ M_\odot, \quad (5)$$

where $\beta \equiv (r_1 - r)/r$. We note that β cannot be arbitrarily large (otherwise the mass in the CSM will diverge), and here we will assume that it is of order unity.

[8] This approximation deviates by a factor of two from a more accurate calculation (e.g., Morrison & McCammon 1983).

By substituting Equation (1) into Equation (4) (assuming $n \approx n_e$) and setting it equal to Equation (5), we can obtain a relation between the mass-loading parameter K, the Hα luminosity, and the radius (Ofek et al. 2013b):

$$L_{H\alpha} \lesssim \frac{4\pi h \nu_H \alpha^{eff} \beta K^2}{\langle \mu_p \rangle m_p^2 r} \approx 2 \times 10^{39} \dot{M}_{0.01}^2 v_{w,500}^{-2} \beta r_{15}^{-1} \text{ erg s}^{-1}. \quad (6)$$

The reason for the inequality is that it is possible that not all of the hydrogen is ionized or that the temperature of the gas is higher than 10^4 K (i.e., $\alpha_{H\alpha}^{eff}$ depends on temperature), and that $\beta > 1$. We note that if $\beta < 1$, then this inequality is incorrect. However, it is reasonable to assume that the width (i.e., $r_1 - r$) of the hydrogen envelope is of the same order of magnitude of r, and therefore $\beta \gtrsim 1$.

Another important caveat (which can be expressed in terms of β) is that unlike the X-ray and radio emission which originate at the shock region (radius r), the narrow component of the Hα may originate at radii $r_{H\alpha} > r$ (i.e., above the shock region). In this case if $L_{H\alpha} \propto \dot{M}_{H\alpha}^2 r_{H\alpha}^{-1}$, then $\dot{M}_{H\alpha}/\dot{M} \approx (r_{H\alpha}/r)^{1/2}$. Therefore, if $r_{H\alpha}$ is an order of magnitude, or more, larger than r, the contribution of $\dot{M}_{H\alpha}$ to the bound–free column density (Equation (2)) and the diffusion timescale discussed in Section 3.4 will be small.

3.3. X-Ray Emission

The X-ray emission from an optically thin region is given by (e.g., Immler et al. 2008)

$$L_X \approx \int_r^\infty 4\pi r^2 \Lambda(T) n^2 dr, \quad (7)$$

where $\Lambda(T)$ is the effective cooling function in the 0.2–10 keV range. Assuming an optically thin thermal plasma with a temperature (T) in the range 10^6–10^8 K (Raymond et al. 1976), we adopt a value of $\Lambda(T) \approx 3 \times 10^{-23}$ erg cm^3 s^{-1}. Substituting Equation (1) into Equation (7), we obtain (e.g., Ofek et al. 2013b)

$$L_X \approx 4\pi \Lambda(T) \frac{K^2}{\langle \mu_p \rangle^2 m_p^2 r} e^{-(\tau+\tau_{bf})} \approx 3.8 \times 10^{41} \dot{M}_{0.01}^2 v_{w,500}^{-2} r_{15}^{-1} e^{-(\tau+\tau_{bf})} \text{ erg s}^{-1}. \quad (8)$$

This expression includes an additional exponential term due to absorption in the wind, where τ is the Thomson optical depth (see Ofek et al. 2010; Balberg & Loeb 2011), which is $\sim 0.3 \dot{M}_{0.01} v_{w,500}^{-1} r_{15}^{-1}$. Although the Thomson optical depth is well known, when the optical depth is of the order of a few, Compton scattering is expected to reprocess more energetic photons into the 0.2–10 keV band (Chevalier & Irwin 2012; Svirski et al. 2012). Since the exact X-ray spectrum is not known (Katz et al. 2011; Svirski et al. 2012), a proper calculation of L_X when $\tau \gtrsim 1$ is not straightforward. Assuming that the Comptonization of hard X-ray band into the soft X-ray band is smaller than the reduction of soft X-ray flux by the optical-depth factors, Equation (8) provides an order of magnitude lower limit on $\dot{M}$.

In Figure 1, the black solid line shows an order-of-magnitude estimate of the expected X-ray luminosity, assuming an optically thin wind-profile CSM with a mass-loss rate of 7×10^{-4} $M_\odot$ yr^{-1} and $v_w = 500$ km s^{-1} (Equations (8) and (12)). Some points are discrepant by factors of 2–3 in luminosity from this estimate. However, this is a simplistic model and since $\dot{M} \propto L_X^{1/2}$, our mass-loss estimate based on the X-ray luminosity is plausibly correct to within an order of magnitude.

We conclude that this formula can be trusted only for $\dot{M} \lesssim 10^{-2}$ $M_\odot$ yr^{-1}. Above this mass-loss rate, τ and τ_{bf} are larger than unity.

3.4. Diffusion Timescale

Another observable that can be used to constrain the mass-loss rate is the rise time of the SN light curve. If a considerable amount of material is present between the SN and the observer, then photon diffusion will slow down the rise time of the SN light curve. Therefore, the maximum observed SN rise time can be used to put an upper limit on the amount of mass between the SN and the observer. The diffusion timescale in an infinite wind profile is given by (e.g., Ginzburg & Balberg 2012)

$$t_{diff} \approx \frac{\kappa K}{c} \left[\ln\left(\frac{c}{v_{sh}}\right) - 1 \right] \cong 0.13 \kappa_{0.34} \dot{M}_{0.01} v_{w,500}^{-1} \left[\ln\left(30 v_{sh,4}^{-1}\right) - 1 \right] \text{ day}. \quad (9)$$

Here, $v_{sh,4}$ is the SN shock velocity in units of 10^4 km s^{-1}. In the case of SN 2009ip, the early fast rise of the SN light curve provides an upper limit on t_{diff} and, therefore, an upper limit on $\dot{M}$.

3.5. Free–free Absorption

Typically, SN progenitors with mass-loss rates of $\sim 10^{-6}$ $M_\odot$ yr^{-1} are easily detectable in radio frequencies in the nearby universe (e.g., Horesh et al. 2013; Krauss et al. 2012). The radio emission is the result of an interaction between the SN shock and the CSM that generates synchrotron radiation peaking at radio frequencies (e.g., Slysh 1990; Chevalier & Fransson 1994; Chevalier 1998). However, if the material is ionized or partially ionized, then the free–free optical depth may block this radiation. The free–free optical depth in a wind profile between radius r and the observer is given by (e.g., Ofek et al. 2013a)

$$\tau_{ff} \approx 1.0 \times 10^5 T_{e,4}^{-1.35} \nu_{10}^{-2.1} v_{w,500}^{-2} \dot{M}_{0.01}^2 r_{15}^{-3}, \quad (10)$$

where ν_{10} is the frequency in units of 10 GHz. We note that the presence of Balmer lines in the spectrum likely means that at least some of the hydrogen is ionized and therefore free–free absorption is important.

Chandra & Soderberg (2012) and Hancock et al. (2012) reported on radio observations of SN 2009ip obtained on 2012 September 26 using the Jansky Very Large Array (JVLA[9]) and the Australia Telescope Compact Array (ATCA). The JVLA observations did not detect the SN in the 22 GHz and 8.9 GHz bands down to a 3σ upper limit of 131 μJy and 65 μJy, respectively. The ATCA observations put a 3σ limit of 66 μJy in the 18 GHz band. Since our previous limits show that there is a significant amount of CSM interacting with the SN shock in this event, it is likely that strong synchrotron radiation is generated. The non-detection of such a radio source implies that $\tau_{ff} > 1$, providing, therefore, a lower limit on $\dot{M}$.

[9] The Jansky Very Large Array is operated by the National Radio Astronomy Observatory (NRAO), a facility of the National Science Foundation operated under cooperative agreement by Associated Universities, Inc.

3.6. Precursor Fluence

Prior to the fast rise detected on 2012 September 24 (Prieto et al. 2013), the light curve of SN 2009ip presented a feature which can be interpreted as $\gtrsim$1 month-long outburst. If we assume that this outburst was a mass-loss event (rather than part of the SN explosion), and if we assume that the bolometric luminosity of the outburst is of the same order of magnitude as the kinetic energy released in the outburst, then by comparing the bolometric luminosity with the kinetic energy we can obtain a rough estimate of the mass released in the outburst. The outburst had a peak absolute V-band magnitude of about -15 and a duration of at least 30 days (see Prieto et al. 2013). Therefore, the total bolometric fluence of the outburst is $E_{\rm bol} \gtrsim 8\times10^{47}$ erg. The reason for the lower limit is that we do not know the outburst light curve bolometric correction,[10] and we only have a lower limit on its duration. Comparing $E_{\rm bol}$ with the kinetic energy and dividing by the duration of the event, $t_{\rm dur}$, we obtain a lower limit on the mass-loss rate

$$\dot{M} \gtrsim \frac{2E_{\rm bol}}{v^2 t_{\rm dur}} \cong 1.6\times10^{-3} v_{\rm w,2000}^{-2} E_{\rm bol,8e47} t_{\rm dur,30}^{-1}\, M_\odot\ {\rm yr}^{-1}, \quad (11)$$

where $v_{\rm w,2000}$ is the wind/outburst velocity in units of 2000 km s^{-1}, $E_{\rm bol,8e47}$ is the bolometric energy in units of 8×10^{47} erg, and $t_{\rm dur,30}$ is the outburst duration in units of 30 days.

4. DISCUSSION

4.1. Constraints on Mass Loss

Along with the observations, Equations (2), (6), (8), (9), (10), and (11) provide order-of-magnitude lower and upper bounds on the mass-loss rate from the SN progenitor. It is important to note that the reason that these are only order-of-magnitude estimates is because some of the assumptions that go into these formulae are likely inaccurate: for example, the assumption that the wind is infinite, continuous, and can be described by a single velocity component or the assumption of spherical symmetry. Nevertheless, these relations provide order-of-magnitude, independent estimators for the SN progenitor mass-loss rate.

Some of the estimators require knowledge regarding the shock radius r. Following Chevalier (1982), we use the approximation[11]

$$r \sim \int v(t)dt = (5/4)v_{\rm ej,s}(t_{\rm s}-t_0)^{1/5}(t-t_0)^{4/5} \approx 3\times10^{15}\frac{v_{\rm ej,s}}{8000\,{\rm km\,s^{-1}}}\left(\frac{t-t_0}{30\,{\rm day}}\right)^{4/5}{\rm cm}, \quad (12)$$

where t is the time, t_0 is the SN explosion time, and $v_{\rm ej,s}$ is the SN ejecta velocity ($\approx$8000 km s^{-1}) at $t_{\rm s}$ ($t_{\rm s}-t_0 = 71$ day). In Figure 4, we present the limits we derive on $\dot{M}$, as a function of the wind/outburst velocity. Specifically, assuming $N \sim N_{\rm H}$, our X-ray observations of SN 2009ip provide an upper limit of $N_{\rm H} < 2\times10^{22}$ cm^{-2}. Therefore, Equation (2) constitutes an upper limit on $\dot{M}$ (black dashed line). Using Equation (6), the Hα line luminosity of the *narrow* Hα component we measured on 2012 December 4, $L_{\rm H\alpha} \approx 1.6\times10^{39}$ erg s^{-1}, and assuming $\beta = 1$, we can set a lower limit on $\dot{M}$ (gray solid line). As discussed in Section 3, Equation (8), along with our measured X-ray luminosity of 1.1×10^{39} erg s^{-1}, sets a lower limit on $\dot{M}$ which is shown as the black solid line in Figure 4. Furthermore, the SN rise time of 2.3 mag day^{-1} (Prieto et al. 2013) implies $t_{\rm diff} \lesssim 0.3$ day. Along with Equation (9) these provide an upper limit on $\dot{M}$ (gray dashed line). The estimate based on the bolometric fluence (Equation (11)) is shown as a vertical gray thick line. The non-detection in radio bands (Chandra & Soderberg 2012; Hancock et al. 2012) with Equation (10) sets a lower limit on $\dot{M}$ (black dash-dotted line). On each line we also mark the $(t-t_0)$ used to calculate the line position. Here we assume that t_0 is on 2012 September 24.

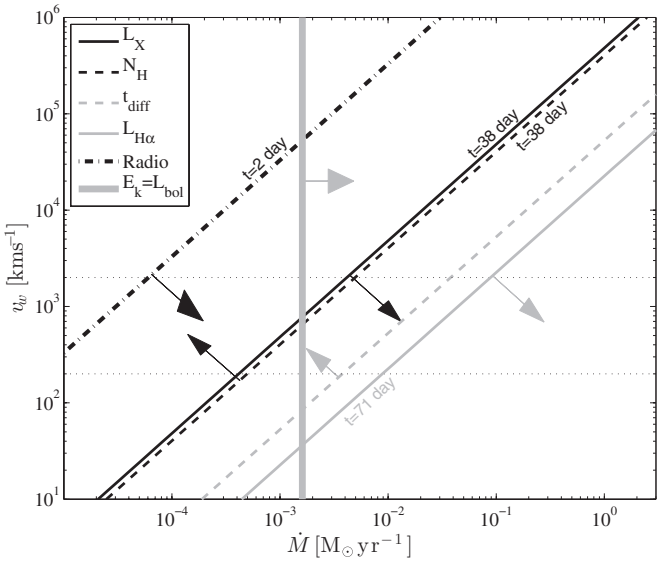

Figure 4. Upper and lower limits on the mass-loss rate of the SN 2009ip progenitor as a function of the wind/outburst velocity. The assumptions that go into these bounds are discussed in Section 3. The solid black line shows the limit based on the X-ray luminosity (Equation (8)). The solid gray line represents the Hα luminosity derived limits (Equation (6)). The black dashed line and the gray dashed line represent the column density (Equation (2)) and diffusion timescale (Equation (9)) limits, respectively. The vertical thick gray solid line is based on the bolometric fluence (Equation (11)). Finally, the free–free absorption limit (Equation (10)) is represented by the black dash-dotted line. The arrow attached to each line marks the direction of the region allowed by the line criteria. The horizontal dotted lines mark the 200 and 2000 km s^{-1} wind/outburst velocity which we derive from the, presumably pre-explosion, IR spectrum (Figure 3). These lines constitute the approximate range of plausible wind/outburst velocities. Since it is likely that the mass loss was not a continuous process with a constant mass-loss rate, these measurements should be regarded as an order-of-magnitude estimate. See discussion in Section 4.

Although there is no single $\dot{M}$ value which is consistent with all the bounds in Figure 4, the closest values to all the bounds are in the range of about 10^{-3} to 10^{-2} $M_\odot$ yr^{-1}.

Kiewe et al. (2012) review the observed properties of 15 Type IIn SNe. They reported mass-loss rates, prior to explosion, in the range of 10^{-4} to $\sim$1 $M_\odot$ yr^{-1}, while their wind velocities are in the range of $\sim$30–1600 km s^{-1}. The mass-loss rate and wind velocity of SN 2009ip are consistent with these values. Another SN which shows some similarities with SN 2009ip is SN 2010mc (PTF 10tel; Ofek et al. 2013b). This SN showed an outburst about one month prior to its explosion. We note that the high state of SN 2009ip just prior to its fast rise (Prieto et al. 2013) can be interpreted as a similar outburst.

[10] The bolometric magnitude correction is always positive.

[11] Assuming that the power-law index describing the ejecta velocity distribution is $m = 8$. Note that Chevalier (1982) denoted this variable by n, while Balberg & Loeb (2011) use m.

Type IIn SNe are likely a non-homogeneous class of objects arising from multiple mechanisms. It is not clear what the best combination of parameters that will help us to relate a given Type IIn to a specific mechanism/progenitor is (e.g., LBV eruptions). However, better mass-loss rates and wind velocity measurements for larger samples of Type IIn SN progenitors, as well as additional cases of pre-explosion outbursts, can provide the missing link.

4.2. Interpretation

With the exception of the mass estimate based on the Hα luminosity, the mass-loss estimators in Figure 4 are consistent to an order of magnitude. Specifically, the mass-loss lower limit based on the Hα luminosity, and assuming $\beta = 1$, is over an order of magnitude above the upper limit which is derived from the bound–free absorption column-density limit. We note that in the case of another source in which a similar analysis was applied (SN 2010mc/PTF 10tel; Ofek et al. 2013b), the various estimators were consistent.

A possible explanation for the discrepancy here is that some of our basic assumptions are incorrect. Among these assumptions are uniformity of the CSM, spherical symmetry, r^{-2} density profile, solar metallicity, and ionized (but not fully ionized) CSM. Alternatively, as we discussed in Section 3.2, it is possible that the Hα emitting region is further out, above the shock region (e.g., $\beta \gg 1$). Therefore, it is possible that the Hα line luminosity probes a completely different region of the CSM than the other methods discussed in Section 3.

Interestingly, we note that in Figure 4 the solution allowed by all the mass-loss rate estimators which depend on the integral of density along the line of sight (marked by non-solid lines in Figure 4) infers low mass-loss rates, while estimators which measure the total emission from an optically thin volume (marked by solid lines in Figure 4) give high values for the mass-loss rate. This behavior hints that another possible explanation for the discrepancy between the various lines in Figure 4 is that the CSM has an aspherical geometry.

There are two simple geometries that are roughly consistent with these results. The first simple explanation is that the CSM around the SN has a disk geometry, and we observe the system from above or below the disk. In this case there will be a relatively small amount of intervening material between the observer and the source, hence the small value of $N_{\rm H}$ and short $t_{\rm diff}$. Moreover, in this case the total emission ($L_{\rm X}$ and $L_{\rm H\alpha}$) will be larger relative to the expectation based on the spherical geometry assumption and on the values of $N_{\rm H}$ and $t_{\rm diff}$. The second simple model is that the CSM has a bipolar hourglass-like structure. In this case we observe the system from the equatorial plane. We note that there are likely other possible geometrical solutions, which are more complicated.

We conclude that the best explanation for the discrepancy between the mass-loss estimators is that the Hα emission region is above the shock region (or effectively $\beta \gg 1$), or alternatively that the CSM is aspherical. Unfortunately, our order-of-magnitude analysis does not provide a way to distinguish between the two scenarios.

If the Hα emission region is indeed located further out, relative to the shock, then an immediate conclusion is that an order-of-magnitude estimate to the mass-loss rate during the SN precursor is in the range of $\sim 10^{-3}\ M_{\odot}\ {\rm yr}^{-1}$ to $\sim 10^{-2}\ M_{\odot}\ {\rm yr}^{-1}$.

In order to convert the mass-loss rate to an estimate of the total mass in the CSM, we need to integrate Equation (5) out to a specific radius. Here we choose to integrate the total mass out to a radius of 6×10^{15} cm. The reason for this choice is that the relatively abrupt disappearance of the X-ray flux $\sim$70 days after the explosion may indicate that the CSM density is falling (faster than a wind profile) at a distance of 6×10^{15} cm (see Equation (12)). Using Equation (5), we find that the total CSM mass out to this radius is

$$M_{\rm CSM} \sim 4 \times 10^{-2} \dot{M}_{0.01} v_{\rm w,500}^{-1} r_{6E15}\ M_{\odot}. \quad (13)$$

Here, r_{6E15} is the radius in units of 6×10^{15} cm.

4.3. Implications

Pastorello et al. (2013) and Mauerhan et al. (2013) suggested that the outbursts of SN 2009ip are due to pulsational pair instability. However, Woosley et al. (2007) predict that the mass loss in pair instability mass ejections would be at least a few solar masses. Unless the geometry is highly aspherical, this theoretically predicted mass loss is high relative to our estimate of the total mass in the CSM (i.e., $\sim$0.1 $M_{\odot}$). Our mass-loss estimate is of the same order of magnitude as the one derived in Ofek et al. (2013b) in the context of the Quataert & Shiode (2012) mechanism. The estimators presented in Figure 4 are also in rough agreement with the shell mass of $\sim$0.15 $M_{\odot}$ suggested by Soker & Kashi (2012), in the context of their binary–star merger scenario.

Interestingly, both Levesque et al. (2012) and Soker & Kashi (2012) suggested aspherical models for SN 2009ip (see also Mauerhan et al. 2013). Levesque et al. (2012) argued for a thin disk geometry, while Soker & Kashi (2012) suggested a bipolar hourglass-like geometry. However, Soker & Kashi (2012) suggested that we are observing the system along the polar direction. We note that if the discrepancy in Figure 4 is due to asymmetry in the CSM, rather than the radius at which the Hα line is generated, then the Soker & Kashi (2012) geometry is not consistent with our observations. However, we do not claim that our suggested geometries are the only possible solutions. Finally, we note that different mass-loss estimators have different functional dependencies on r. Therefore, additional observations (e.g., radio) can constrain the density profile of the CSM.

We thank Orly Gnat, Udi Nakar, Stan Woosley, Nir Sapir, and Avishay Gal-Yam for productive discussions, and an anonymous referee for useful suggestions. We gratefully acknowledge the collaboration of the XMM Project team, and in particular Dr. Norbert Schartel, for the XMM ToO observations. E.O.O. is incumbent of the Arye Dissentshik career development chair and is grateful to support by a grant from the Israeli Ministry of Science. M.M.K. acknowledges generous support from the Hubble Fellowship and Carnegie-Princeton Fellowship.

REFERENCES

Arnett, W. D., & Meakin, C. 2011, ApJ, 741, 33
Balberg, S., & Loeb, A. 2011, MNRAS, 414, 1715
Behar, E., Dado, S., Dar, A., & Laor, A. 2011, ApJ, 734, 26
Campana, S. 2012, ATel, 4444, 1
Chandra, P., & Soderberg, A. M. 2012, ATel, 4433, 1
Chevalier, R. A. 1982, ApJ, 259, 302
Chevalier, R. A. 1998, ApJ, 499, 810
Chevalier, R. A. 2012, ApJL, 752, L2
Chevalier, R. A., & Fransson, C. 1994, ApJ, 420, 268
Chevalier, R. A., & Irwin, C. M. 2012, ApJL, 747, L17
Chugai, N. N., Blinnikov, S. I., Cumming, R. J., et al. 2004, MNRAS, 352, 1213
Chugai, N. N., & Danziger, I. J. 1994, MNRAS, 268, 173

Dickey, J. M., & Lockman, F. J. 1990, ARA&A, 28, 215
Dopita, M. A., Cohen, M., Schwartz, R. D., & Evans, R. 1984, ApJL, 287, L69
Drake, A. J., Howerton, S., McNaught, R., et al. 2012, ATel, 4334, 1
Drake, A. J., Prieto, J. L., Djorgovski, S. G., et al. 2010, ATel, 2897, 1
Filippenko, A. V. 1997, ARA&A, 35, 309
Foley, R. J., Berger, E., Fox, O., et al. 2011, ApJ, 732, 32
Foley, R. J., Smith, N., Ganeshalingam, M., et al. 2007, ApJL, 657, L105
Gal-Yam, A., & Leonard, D. C. 2009, Natur, 458, 865
Gal-Yam, A., Leonard, D. C., Fox, D. B., et al. 2007, ApJ, 656, 372
Gehrels, N., Chincarini, G., Giommi, P., et al. 2004, ApJ, 611, 1005
Ginzburg, S., & Balberg, S. 2012, arXiv:1205.3455
Hancock, P., Bannister, K., & Bell, M. 2012, ATel, 4434, 1
Horesh, A., Stockdale, C., Fox, D. B., et al. 2013, ApJ, submitted (arXiv:1209.1102)
Immler, S., Modjaz, M., Landsman, W., et al. 2008, ApJL, 674, L85
Katz, B., Sapir, N., & Waxman, E. 2011, arXiv:1106.1898
Kiewe, M., Gal-Yam, A., Arcavi, I., et al. 2012, ApJ, 744, 10
Kochanek, C. S., Szczygiel, D. M., & Stanek, K. Z. 2011, ApJ, 737, 76
Kochanek, C. S., Szczygieł, D. M., & Stanek, K. Z. 2012, ApJ, 758, 142
Krauss, M. I., Soderberg, A. M., Chomiuk, L., et al. 2012, ApJL, 750, L40
Levesque, E. M., Stringfellow, G. S., Ginsburg, A. G., Bally, J., & Keeney, B. A. 2012, arXiv:1211.4577
Margutti, R., & Soderberg, A. 2012, ATel, 4457, 1
Margutti, R., Soderberg, A., & Milisavljevic, D. 2012, ATel, 4414, 1
Mauerhan, J. C., Smith, N., Filippenko, A., et al. 2013, MNRAS, 430, 1801
Maza, J., Hamuy, M., Antezana, R., et al. 2009, CBET, 1928, 1
Moretti, A., Campana, S., Tagliaferri, G., et al. 2004, Proc. SPIE, 5165, 232
Morrison, R., & McCammon, D. 1983, ApJ, 270, 119
Ofek, E. O., Cameron, P. B., Kasliwal, M. M., et al. 2007, ApJL, 659, L13
Ofek, E. O., Fox, D., Cenko, S. B., et al. 2013a, ApJ, 763, 42
Ofek, E. O., Rabinak, I., Neill, J. D., et al. 2010, ApJ, 724, 1396
Ofek, E. O., Sullivan, M., Cenko, S. B., et al. 2013b, Natur, 494, 65
Osterbrock, D. E., & Ferland, G. J. 2006, in Astrophysics of Gaseous Nebulae and Active Galactic Nuclei, ed. D. E. Osterbrock & G. J. Ferland (2nd ed.; Sausalito, CA: University Science Books)
Pastorello, A., Cappellaro, E., Inserra, C., et al. 2013, ApJ, 767, 1
Pastorello, A., Mattila, S., Zampieri, L., et al. 2008, MNRAS, 389, 113
Prieto, J. L., Brimacombe, J., Drake, A. J., & Howerton, S. 2013, ApJL, 763, L27
Quataert, E., & Shiode, J. 2012, MNRAS, 423, L92
Rakavy, G., Shaviv, G., & Zinamon, Z. 1967, ApJ, 150, 131
Raymond, J. C., Cox, D. P., & Smith, B. W. 1976, ApJ, 204, 290
Schafer, R. A. 1991, XSPEC, An X-ray Spectral Fitting Package: Version 2 of the User's Guide (ESA TM, 1013-7076; Paris, France: European Space Agency)
Simcoe, R. A., Burgasser, A. J., Bernstein, R. A., et al. 2008, Proc. SPIE, 7014, 70140U
Simcoe, R. A., Burgasser, A. J., Bochanski, J. J., et al. 2010, Proc. SPIE, 7735, 773514
Slysh, V. I. 1990, SvAL, 16, 339
Smith, N., Chornock, R., Li, W., et al. 2008, ApJ, 686, 467
Smith, N., Li, W., Foley, R. J., et al. 2007, ApJ, 666, 1116
Smith, N., Li, W., Silverman, J. M., Ganeshalingam, M., & Filippenko, A. V. 2011, MNRAS, 415, 773
Smith, N., & Mauerhan, J. 2012, ATel, 4412, 1
Smith, N., Mauerhan, J. C., Kasliwal, M. M., & Burgasser, A. J. 2013, arXiv:1303.0304
Smith, N., Miller, A., Li, W., et al. 2010, AJ, 139, 1451
Smith, N., Silverman, J. M., Chornock, R., et al. 2009, ApJ, 695, 1334
Soker, N., & Kashi, A. 2012, arXiv:1211.5388
Soker, N., & Kashi, A. 2013, ApJL, 764, L6
Svirski, G., Nakar, E., & Sari, R. 2012, ApJ, 759, 108
Vacca, W. D., Cushing, M. C., & Rayner, J. T. 2003, PASP, 115, 389
Van Dyk, S. D., & Matheson, T. 2012, Eta Carinae and the Supernova Imposters, Astrophysics and Space Science Library, Vol. 384 (Berlin: Springer), 249
Waldman, R. 2008, ApJ, 685, 1103
Woosley, S. E., Blinnikov, S., & Heger, A. 2007, Natur, 450, 390
Yaron, O., & Gal-Yam, A. 2012, PASP, 124, 668